Quaternary Geochronology 6 (2011) 10–21

Contents lists available at ScienceDirect

Quaternary Geochronology

journal homepage: www.elsevier.com/locate/quageo

Research Paper

Cosmogenic ^{3}He production rates in apatite, zircon and pyroxene inferred from Bonneville flood erosional surfaces

William H. Amidon*, Kenneth A. Farley

California Institute of Technology, Geological and Planetary Sciences Division, 1200 E. California Blvd., Pasadena, CA 91125, USA

ARTICLE INFO

Article history:
Received 4 January 2010
Received in revised form
24 March 2010
Accepted 30 March 2010
Available online 7 April 2010

Keywords:
Helium
^{3}H
Tritium
Shoshone Falls
Twin Falls
Li
Thermal neutron

ABSTRACT

^{3}He concentrations were measured in zircon, apatite and pyroxene separates from rhyolite surfaces along the Snake River near Twin Falls, Idaho. These fluted and potholed surfaces were presumably scoured by the Bonneville outburst flood ~17.5 ka. Several of the samples contain inherited ^{3}He from prior exposure, reflecting the complex incision history of the Snake River canyon and suggesting earlier flood events. Each individual mineral from the remaining surfaces yielded ^{3}He concentrations that are within error of each other. ^{3}He produced by neutron capture on ^{6}Li was established from shielded samples and a simple neutron production model. The remaining ^{3}He is spallogenic and was used to calibrate the production rate of cosmogenic ^{3}He in zircon, apatite and pyroxene by assuming minimal erosion since the Bonneville flood. In all three phases the resulting production rates are ~7–12% lower than previous ^{3}He production rate estimates obtained by reference to various production rates for ^{10}Be in quartz. This disagreement is partially reconciled here by recalculating previous results with a ^{10}Be production rate of 4.51 at $g^{-1}\,a^{-1}$ in quartz. Adopting this revised rate brings three independent ^{3}He production rate estimates for zircon and apatite into agreement within 5%, with grand means of 103 ± 3 at $g^{-1}\,a^{-1}$ in zircon and 133 ± 6 at $g^{-1}\,a^{-1}$ in apatite. The major source of uncertainty in cosmogenic ^{3}He dating of these phases is now correction for ^{3}He produced by neutron capture on ^{6}Li. Calculations are presented for assessing the amount of uncertainty introduced by this correction as a function of Li concentration, cosmic-ray exposure age, and He closure age.

1. Introduction

Cosmogenic nuclide dating of terrestrial surfaces provides a powerful tool with which to study the timing and rate of landscape change. This includes applications as varied as the dating of glacial moraines, establishing slip-rates on faults, measuring the erosion rates of basins, and measuring the rates of soil formation (Brook et al., 1993; Bierman et al., 1995; Bierman and Steig, 1996; Heimsath et al., 1997). Although many important questions have been answered, others remain unanswered, in part due to limitations on the number of samples that can typically be analyzed in studies using ^{10}Be, ^{26}Al, and ^{36}Cl. In contrast, rapid preparation and analysis of samples for cosmogenic ^{3}He often allows a greater number of samples to be analyzed, but the application of cosmogenic ^{3}He dating has so far been limited primarily to olivine and pyroxene. Because ^{3}He is produced in all mineral phases, it can potentially be applied in almost any lithology. This study demonstrates the potential of ^{3}He dating in zircon and apatite to constrain geomorphic histories in study areas which lack quartz for ^{10}Be, ^{26}Al, or ^{21}Ne dating. In addition, we present a new calibration of ^{3}He production rates, which agree to within 5% with the revised results from two previous studies.

Part of the reason that cosmogenic ^{3}He has been relatively under-utilized is that calibration studies, and thus applications, have usually been limited to pyroxene or olivine in young lava flows (Cerling and Craig, 1994; Licciardi et al., 1999, 2006; Dunai and Wijbrans, 2000; Ackert et al., 2003; Blard et al., 2006). Because these studies have been performed at a range of elevations and latitudes, the best estimate of the production rate is dependent upon the scaling scheme that is used to convert local measurements to production rates at sea-level high-latitude (SLHL). A compilation of existing calibration studies performed against ^{14}C or ^{40}Ar/^{39}Ar ages of uneroded surfaces gives SLHL production rates between ~115 and 133 at $g^{-1}\,a^{-1}$ for olivine and pyroxene, with a ~10% standard deviation when a given scaling model is applied (Goehring et al., 2010). More recent studies have focused on inter-isotope calibrations, comparing ^{3}He in pyroxene, olivine, garnet, zircon, apatite, and titanite against ^{10}Be in quartz (Gayer et al., 2004; Amidon et al., 2008, 2009; Niedermann et al., 2009). These studies have yielded ^{3}He production rates that are systematically

* Corresponding author. Tel.: +1 626 395 2190.
E-mail address: wamidon@gps.caltech.edu (W.H. Amidon).

1871-1014/$ – see front matter © 2010 Elsevier B.V. All rights reserved.
doi:10.1016/j.quageo.2010.03.005

higher than those estimated from calibrations against ^{14}C or $^{40}Ar/^{39}Ar$. One proposed explanation for this disagreement is that these inter-isotope calibrations have focused on crustal rocks that are high in Li. In such rocks excess ^{3}He from neutron capture on ^{6}Li could account for the discrepancy (Dunai et al., 2007) especially in the absence of shielded samples for establishing baseline ^{3}He level. While this possibility has been refuted, the role of ^{6}Li is clearly important and is not yet fully understood (Amidon et al., 2008, 2009).

The goals of this study are to calibrate ^{3}He production rates in zircon, apatite and pyroxene independently of ^{10}Be, and to use shielded samples to better document Li-produced ^{3}He components. We thus present ^{3}He measurements from zircon, apatite, and pyroxene from shielded and surface exposed samples that have been scoured by the Bonneville outburst flood near Twin Falls, Idaho. This is an ideal calibration site because the timing of the flood is known from numerous ^{14}C ages and has been used in several previous cosmogenic production rate studies (Cerling, 1990; Handwerger et al., 1999; Lifton et al., 2001, 2009; Goehring et al., 2010). The site also lies within ~700 km of many calibration sites in the western US, which reduces scaling-related uncertainties when these studies are compared (Cerling and Craig, 1994; Licciardi et al., 1999; Amidon et al., 2009; Goethals et al., 2009). Our results show that although Li-produced ^{3}He exists in most samples, the use of shielded samples allows subtraction of this component with reasonable precision. This study yields spallation ^{3}He production rates of 117–139, 123–146, and 96–113 at $g^{-1}\,a^{-1}$ (1σ uncertainties) for pyroxene, apatite, and zircon, depending upon what scaling scheme is adopted (Balco et al., 2008). The pyroxene result is in agreement with previous production rates obtained by direct dating of geomorphic surfaces. Although the zircon and apatite data are lower than previously published values, this discrepancy is largely reconciled by adopting a revised ^{10}Be production rate of 4.51 at $g^{-1}\,a^{-1}$.

2. Geologic background and sampling

The study area is near Twin Falls, Idaho where the Snake River has carved a canyon through which waters of the Bonneville outburst flood passed at ~17.5 ka (Fig. 1). Detailed mapping of flood deposits suggests that the floodwaters split into two channels, with ~300,000 m^3/s transported as bank-full flow through the main canyon and ~600,000 m^3/s in the Eden overland channel that exited the canyon near Rupert, Idaho and rejoined just below Perrine bridge (O'Connor, 1993). The confluence of these two channels is coincident with an abrupt widening of the canyon, as well as the occurrence of a large amphitheatre-headed side canyon (the Blue Lakes Alcove) and a massive hydraulically scoured "pothole" (Malde, 1968). Although several authors have proposed that these are the result of the Bonneville flood, our results as well as those from recent studies suggest that these features, and similar features nearby, may have formed during earlier flood events (Cerling et al., 1994; Lamb et al., 2008).

The Bonneville flood was released when the alluvium damming the lake at its overflow was abruptly stripped at ~17.5 ka, and the lake level dropped ~100 m to the Provo-stage. The exact timing is established by comparing the youngest Bonneville stage shoreline ages with the oldest Provo-stage shorelines. Reviews of the Bonneville chronology are given in Godsey et al. (2005) and Oviatt et al. (1992). The two youngest ages from the Bonneville stage are 15.3 and 15.1 ^{14}C ka BP, derived from charcoal and wood respectively (Scott et al., 1983; Oviatt et al., 1992). More recently, three identical ages of 15.1 ^{14}C BP were obtained from three separate mollusk samples from sites just below the Bonneville shoreline (Godsey et al., 2005). The oldest ages associated with the Provo shoreline are both 14.3 ^{14}C ka BP, and are derived from inorganic carbon extracted from tufa and from a mollusk (Oviatt, 1991; Light, 1996). Conversion to calendar years gives 2σ age ranges of 17.5–18.5 ka for the oldest Bonneville ages, and 16.5–17.5 ka for the youngest Provo age, from which we adopt an age of 17.5 ± 1 ka for the Bonneville flood event (Godsey et al., 2005; Goehring et al., 2010).

At Twin Falls, the Snake River incises the ~5.7 Ma Shoshone Falls rhyolite and capping Pliocene basalt flows (Armstrong et al., 1975; Bonnichsen et al., 2008). We divide the Shoshone Falls rhyolite into two units, with the lower unit being a green to gray plagioclase–pyroxene rhyolite. This is overlain by a darker colored rhyolite containing plagioclase, two distinct pyroxenes, and abundant fine grained magnetite. Both units contain abundant zircon and apatite, with zircons tending to be large (>75 μm in cross section) and apatites tending to be very small (<75 μm). At Pillar Falls (Fig. 1) we collected two exposed samples from the upper unit (2 and 6), as well as two exposed samples and one shielded sample from the lower unit (4, 5, and 8). The shielded sample was taken from a deep

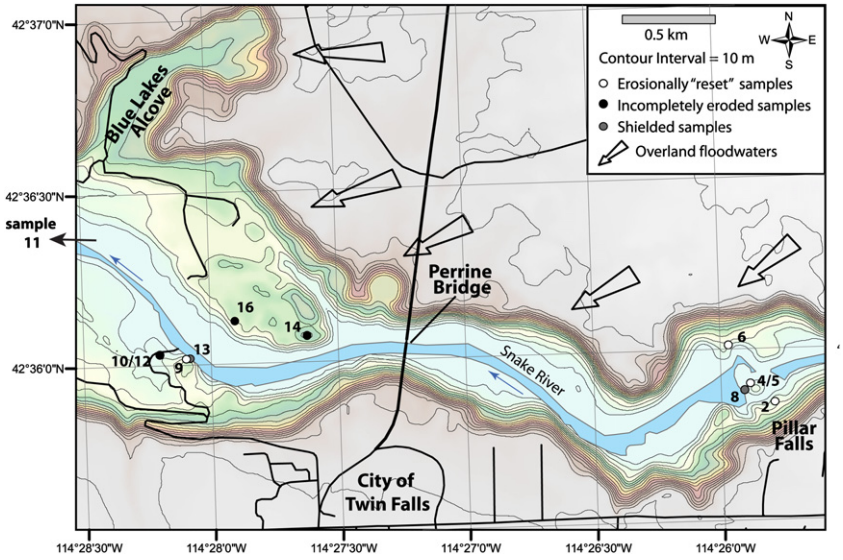

Fig. 1. Topographic map of the Snake River canyon near Twin Falls, Idaho. Circular symbols represent sampling localities, labeled with sample number and shaded according to their inferred erosional history (see text).

cave scoured ~5 m laterally into the central pillar, and sitting ~18 m directly below the surface locations of samples 4 and 5. The latitude, longitude, and elevation of all samples are given in Table 1.

Downstream of Perrine Bridge the widened section of canyon is characterized by well-preserved scour surfaces sitting ~40–60 m above the modern river, and fields of large boulders ("melon gravels") deposited on lower elevation surfaces, typically 5–15 m above the modern river (Fig. 1). We sampled three scour surfaces in the upper unit (9, 14, and 16), as well as a shielded sample (13) and two scour surfaces in the lower unit (9 and 10). The shielded sample was situated beneath ~40 m of overburden and ~1.5 m horizontally from a planar vertical cliff face. Sample 11 was collected from the top of a 4 × 2.5 × 3 m flood-deposited boulder of the lower unit lithology, deposited ~2 km downstream from Perrine bridge. Because the upper lithology is composed of a fine grained matrix, all of the samples collected from this lithology (2, 6, 9, 12, 14, and 16) exhibited patina surfaces preserving scour flutes and/or 5–30 cm wide scour pot-holes. In contrast, surfaces from the lower unit (4, 5, and 11) were partially disaggregated with poor preservation of primary scour features. All of the exposed samples were 4–5 cm thick, and were collected from nearly horizontal surfaces with no topographic shielding. We therefore do not apply shielding corrections of any kind.

3. Methods

Rocks were crushed, sieved to <300 μm, and rinsed before being separated using standard heavy liquid and magnetic techniques. Resulting apatite and zircon separates were wet-sieved into increments of 30–50, 50–75, 75–125, and >125 μm. However, apatite separates were intact and pure enough only for the 50–75 μm size fraction. Likewise, only pyroxenes from the >190 μm fraction were analyzed. Pyroxene separates were leached in an ultrasonic bath in 10% HF:HNO_3 solution for ~1 hour, whereas zircon was purified in a concentrated HF:HNO_3 solution for 3–4 h. All samples were visually inspected and picked free of contaminant phases prior to analysis. Mean grain size was determined by photographing the sample prior to loading, and measuring length and width of >150 representative grains per sample. Because the mean grain sizes computed for given sieve fractions are consistent to within ~2–3 μm between samples, a constant value is reported for each size fraction and is used in all calculations. Typically 20–40 mg of uncrushed zircon and apatite was loaded into platinum capsules. In some cases, pyroxene was crushed under vaccum in a steel tube following previously published procedures (Patterson et al., 1997). To ensure that all grains were uniformly crushed prior to fusion, all pyroxene samples were ground in a mortar and pestle and sieved through a <26 μm sieve prior to loading in Al-foil.

Table 1
Sample locations.

Sample	Lat.	Lon.	Elev. (m)
ID1	42.59605	114.39865	1031
ID2	42.59737	114.42984	991
ID3	42.59865	114.43051	959
ID4/5	42.59829	114.43139	980
ID6	42.60018	114.43277	978
ID8	42.59822	114.4319	962
ID9	42.60026	114.46827	1005
ID11	42.62359	114.5143	960
ID12	42.60051	114.47002	975
ID13	42.60028	114.46803	954
ID14	42.60126	114.46031	1021
ID16	42.60205	114.46501	993

Coordinates relative to WGS 84 datum. Rim of canyon at ~1100 m elevation.

Zircon and apatite crystals were degassed by heating platinum packets to >1100 °C for 30 minutes using a 1064 nm Nd:YAG laser similar to previously published procedures (House et al., 2000; Amidon et al., 2008). Pyroxene powder was degassed for 20 min at 1300 °C in a double-walled resistance furnace. Re-extracts at the same temperature were performed using both techniques and confirmed complete extraction of He from the samples. He gas was purified over an activated charcoal trap at 77 K and over hot and cold Ti SAES getters before being cryogenically focused at 14 K. Helium was released at 32 K into an MAP 215-50 noble gas mass spectrometer. For low ^{4}He analyses (apatite and pyroxene), sensitivity was determined by measuring aliquots of both the Caltech "Air" and "MM" standards of similar size to the sample being analyzed (Poreda and Farley, 1992). For high ^{4}He analyses (zircon) sensitivity was determined by in-run spiking of samples with the "MM" standard, which causes a significant increase in ^{3}He, while only raising the total He pressure by <1% (Amidon et al., 2008). ^{3}He is collected in pulse mode on an electron multiplier whereas ^{4}He is measured on a Faraday cup. Very high ^{4}He concentrations in zircon were determined on an aliquot of the sample gas by peak height measurement on a Balzers Prisma quadropole mass spectrometer. Analytical uncertainty for individual ^{3}He analyses is dominated by counting statistics on the ^{3}He signal and is typically ~10% for zircon, ~8% for apatite and ~7% for pyroxene (1σ). We improve on these precision figures by making replicate analyses. Uncertainty on ^{4}He analyses is dominated by the standardization of the instrument, and is 1–2%, based on the calibration performed when filling the standard tank.

Lithium measurements were made on an Agilent 7500 series ICPMS using isotope dilution with a ^{6}Li spike calibrated with a commercial Li normal solution. Measurements were made on ~1 mg of handpicked material, but not the same aliquots used for ^{3}He analysis. Most samples were dissolved on a hot plate in a 2:1 HF:HNO_3 cocktail except for zircons, which were Parr bombed in HF, redissolved in HCl, and finally in HNO_3. Reproducibility of Li measurements was established by performing at least two replicate measurements on separately picked aliquots of each sample. Lithium blanks typically total less than 0.1% of measured lithium, with a maximum of ~2%. The sample cleaning procedure, and a 1σ external precision of ~6% are established and discussed by Amidon et al. (2008). In some cases, U and Th concentrations were determined on the same samples as Li by removing an aliquot and spiking it for U and Th analyses. U blanks ranged from 0.1 to 1%, and Th blanks ranged from 1 to 3% of measured concentrations. All U and Th analyses were replicated to better than 5% (1σ).

Bulk rock geochemistry was measured on powdered rock samples (~500 g each) that were subsampled and flux melted into glass disks. Major element concentrations were determined by XRF whereas trace elements and REE's were measured by LA-ICPMS following standard procedures at the Michigan State University laboratory (Vogel et al., 2008). Compositions of individual mineral phases were determined using the JEOL JXA-8200 electron microprobe at Caltech.

4. Results

Measured helium concentrations for zircon, apatite, and pyroxene are presented in Tables 2–5. Six of the nine surface exposure samples yield ^{3}He concentrations in zircon that are within error of each other, suggesting that they share a common exposure history. The same is true for the apatite analyses from these 6 samples. The remaining surface exposure samples yield significantly higher ^{3}He concentrations in all phases suggesting that they have retained ^{3}He from exposure prior to the Bonneville flood. Throughout the remainder of this paper, the six samples with

Table 2
Zircon helium results.

	n	^3He_m (Mat/g)	1σ (Mat/g)	^4He (Tat/g)	1σ (Tat/g)	$^3He/^4He$ (Ra*1000)	MER (μm)	$^3He_{sp+cn}$ (Mat/g)	$^3He_{cn}$ (Mat/g)	$1\sigma_{cn}$ (Mat/g)	$^3He_{sp}$ (Mat/g)	1σ (Mat/g)	^3He PR (at g^{-1} a^{-1})	1σ (at g^{-1} a^{-1})
"Reset" surfaces and shielded samples														
<50 μm														
ID5	2	7.3	0.5	3771	420	1.4	27	5.5	0.6	0.1	4.8	0.6	130	33
ID6	1	6.3	0.6	3760	380	1.2	27	4.4	0.6	0.1	3.8	0.7	102	38
ID11	2	6.9	0.5	5286	604	0.9	27	5.1	0.6	0.1	4.4	0.5	120	31
Weighted mean		***6.8***	***0.4***								***4.4***	***0.4***	***119***	***25***
ID8 (S)	2	1.5	0.2	4254	835	0.2	27	–	–	–	–	–	–	–
ID13 (S)	3	2.2	0.2	3004	535	0.4	27	–	–	–	–	–	–	–
Shielded mean		**1.8**	**0.2**											
50 – 75 μm														
ID2	1	5.5	0.6	3306	356	1.2	38	3.9	0.5	0.1	3.6	0.6	97	33
ID4	3	6.8	0.4	3732	475	1.3	38	5.2	0.5	0.1	4.9	0.4	134	25
ID5	4	5.8	0.3	3590	535	1.2	38	4.2	0.5	0.1	3.8	0.3	104	20
ID6	1	5.6	0.6	3167	339	1.3	38	4.0	0.5	0.1	3.6	0.6	99	33
ID9	2	5.3	0.4	3172	414	1.2	38	3.7	0.5	0.1	3.4	0.4	92	24
ID11	2	6.6	0.5	3862	454	1.2	38	4.9	0.5	0.1	4.6	0.5	126	29
Weighted mean		***5.9***	***0.3***								***4.0***	***0.3***	***109***	***19***
ID8 (S)	3	1.6	0.1	3454	721	0.3	38	–	–	–	–	–	–	–
ID13 (S)	5	1.6	0.1	3525	827	0.3	38	–	–	–	–	–	–	–
Shielded mean		**1.6**	**0.1**											
75 – 100 μm														
ID4	3	5.2	0.3	3543	517	1.1	55	4.0	0.3	0.0	3.8	0.3	102	20
ID5	2	5.3	0.4	3189	418	1.2	55	4.0	0.3	0.0	3.8	0.4	104	23
ID6	3	5.3	0.3	3256	471	1.3	55	4.1	0.3	0.0	3.9	0.3	105	20
ID9	1	5.2	0.5	3204	355	1.2	55	4.0	0.3	0.0	3.8	0.5	102	31
ID11	1	5.9	0.6	3287	342	1.3	55	4.7	0.3	0.0	4.5	0.6	121	35
Weighted mean		***5.4***	***0.1***								***3.9***	***0.2***	***105***	***13***
ID8 (S)	2	1.2	0.1	3506	765	0.2	55	–	–	–	–	–	–	–
ID13 (S)	5	1.3	0.1	3643	953		55	–	–	–	–	–	–	–
Shielded mean		**1.2**	**0.1**											
>100 μm														
ID4	1	5.1	0.5	3700	415	1.0	105	4.3	0.2	0.0	4.2	0.5	115	31
ID5	2	4.4	0.3	3683	530	0.9	105	3.6	0.2	0.0	3.5	0.3	95	20
ID6	2	4.8	0.3	3300	452	1.1	105	4.0	0.2	0.0	4.0	0.4	108	22
ID9	2	4.9	0.3	3333	453	1.1	105	4.1	0.2	0.0	4.0	0.4	110	22
ID11	2	4.5	0.3	3566	505	0.9	105	3.7	0.2	0.0	3.7	0.3	100	20
Weighted mean		***4.7***	***0.1***								***3.8***	***0.2***	***104***	***11***
ID8 (S)	2	0.7	0.1	3635	1046	0.1	105	–	–	–	–	–	–	–
ID13 (S)	1	0.9	0.1	3977	850	0.2	105	–	–	–	–	–	–	–
Shielded mean		**0.8**	**0.1**											
Grand mean (>37 μm)											***3.9***	***0.1***	***105***	***9***
"Unreset" surfaces														
ID12 (50–75)	1	23.4	1.9	3076	180	5.5	38	21.8	3.2	0.4	19.1	1.9	–	–
ID12 (75–125)	2	27.5	1.6	3200	205	6.5	55	26.3	2.8	0.4	23.3	1.6	–	–
ID14 (<75)	1	9.5	0.8	3058	281	2.2	38	7.9	1.2	0.2	7.3	0.8	–	–
ID14 (75–100)	1	10.7	0.9	3421	296	2.2	55	9.4	1.0	0.1	8.3	0.9	–	–
ID16 (50–75)	1	23.6	1.9	3438	200	4.9	38	22.0	3.2	0.4	19.0	1.9	–	–
ID16 (75–100)	3	23.0	1.1	3141	244	5.4	55	21.8	2.3	0.3	19.6	1.1	–	–
ID16 (>100)	1	22.5	1.8	3881	231	4.2	105	21.7	1.4	0.2	20.4	1.8	–	–

(S) denotes shielded samples; n = # of replicate analyses; 1σ = standard error, MER = mean equivalent radius; $1\sigma_{cn}$ = Monte Carlo standard deviation on $^3He_{cn}$ component; ^3He_m = measured; $^3He_{cn}$ = modeled ^3He from ^6Li and cosmogenic neutrons; $^3He_{sp}$ = net spallation after subtraction of Li-produced components. Production rates are determined using a scaling factor of 2.1 and assumed age of 17,500 ± 500 yrs (1σ) for Bonneville flood event.

similar concentrations will be referred to as "reset surfaces" and, the 3 samples with high ^3He will be referred to as the "unreset surfaces," reflecting their incomplete erosional resetting during the flood.

Measured ^3He concentrations in zircons from reset surfaces are ~6 Mat/g compared to as much as 28 Mat/g in unreset surfaces (Table 2). Concentrations of ^3He in the two shielded samples agree within error at ~1.5 Mat/g. Both shielded and exposed zircons show an increase in ^3He concentration with decreasing grain size. For reset samples this typically amounts to about a 30% increase between the >100 μm and <50 μm size fractions (Fig. 2). Apatites from the 50–75 μm size fraction yielded consistently higher ^3He concentrations than in zircons of the same size, with ~9 Mat/g for reset surfaces and up to 29 Mat/g for unreset surfaces (Table 3). Shielded apatites contain ~3.4 Mat/g of ^3He. Results of two apatite crushing experiments yielded $^3He/^4He$ ratios of 0.01 Ra, suggesting no detectable mantle (~8 Ra) helium (Table 5).

Although both Fe-rich and Fe–Ca pyroxenes were present in most samples (Online Table 1), only pyroxenes with the Fe–Ca composition, $(Mg_{0.62}Fe_{0.58}Ca_{0.74})Si_2O_6$, were analyzed for ^3He. Concentrations of ^3He in pyroxene from reset surfaces range from ~7–11 Mat/g and show a strong correlation with Li content (Table 4). ^3He concentrations in unreset samples reach 38 Mat/g. The average ^4He concentration is 57 ± 14 Tat/g, giving relatively radiogenic $^3He/^4He$ ratios of 0.1–0.5 Ra. Results from crushing experiments show that the trapped helium component is

Table 3
Apatite helium results.

	n	^3He_m (Mat/g)	1σ (Mat/g)	^4He (Tat/g)	1σ (Tat/g)	$^3He/^4He$ (Ra*1000)	MER (μm)	$^3He_{sp+cn}$ (Mat/g)	$^3He_{cn}$ (Mat/g)	$1\sigma_{cn}$ (Mat/g)	$^3He_{sp}$ (Mat/g)	1σ (Mat/g)	^3He PR (at g^{-1} a^{-1})	1σ (at g^{-1} a^{-1})
"Reset" surfaces and shielded samples														
ID4	1	9.8	0.8	1207	60	4	36	6.4	0.9	0.1	5.5	0.8	151	74
ID5	2	9.2	0.7	1151	58	6	36	5.9	0.9	0.1	5.0	0.8	136	59
ID6	2	8.9	0.7	1288	64	5	36	5.6	0.7	0.1	4.9	0.7	133	32
ID9	2	9.0	0.7	711	36	10	36	5.6	0.7	0.1	4.9	0.7	135	54
ID11	1	8.7	0.7	889	44	7	36	5.3	0.9	0.1	4.5	0.7	122	35
Mean		***9.1***	***0.2***					***5.8***			***4.9***	***0.3***	***135***	***17***
Shielded samples														
ID8 (s)	3	3.2	0.3	796	40	3	36	–	–			–	–	–
ID13 (s)	4	3.5	0.3	609	30	4	36	–	–			–	–	–
Shielded mean		***3.4***	***0.1***											
"Unreset" surfaces														
ID12	1	29.0	2.3	984	49	21	36	25.6	3.8	0.6	21.8	2.4	–	–
ID14	2	14.1	1.1	833	42	13	36	10.7	1.6	0.3	9.1	0.8	–	–
ID16	2	23.3	1.9	1067	53	16	36	19.9	2.5	0.4	17.4	1.4	–	–

n = # of replicate analyses; 1σ = standard error, MER = mean equivalent radius; $1\sigma_{cn}$ = Monte Carlo standard deviation on $^3He_{cn}$ component; ^3He_m = measured; $^3He_{cn}$ = modeled ^3He from ^3Li and cosmogenic neutrons; $^3He_{sp}$ = net spallation ^3He after subtraction of Li-produced components. Production rates are determined using a scaling factor of 2.1 and assumed age of 17,500 ± 500 yrs (1σ) for Bonneville flood event.

distinctly different between pyroxene from the upper and lower units but is less than 4% of matrix-sited ^3He concentrations in all cases (Table 4). Results from crushing experiments reproduce well, suggesting that complete extraction of magmatic gasses was achieved.

Major element compositions of the upper and lower rhyolite units are nearly identical despite their significant textural variations (Online Table 2). However, bulk rock Li concentrations are significantly different between the two units, with ~15 ppm in the upper unit and ~21 ppm in the lower unit (Table 6). The contrast in Li contents between the upper and lower units is magnified in the pyroxenes. Those from the upper unit contain 16–25 ppm of Li, whereas those from the lower unit contain 34–90 ppm. The Li concentrations vary widely across small spatial scales, with three samples collected within ~5 m of each other (4, 5, and 8) giving concentrations of 34, 53, and 90 ppm. Li variations in other mineral phases are less significant, ranging from 1 to 2 ppm in zircon and from 3 to 8 ppm in apatite. Bulk rock U and Th concentrations are similar in both units at ~6 and 17 ppm respectively, and are ~250 and ~120 ppm in zircon, and ~0.1 and 0.3 ppm in pyroxene (Table 6).

5. Analysis

5.1. The nucleogenic ^3He component in shielded samples

The presence of matrix-sited ^3He in our shielded samples is due primarily to production via capture of radiogenic neutrons on ^6Li in the reaction $^6Li(n,\alpha)^3H \rightarrow {}^3He$. This is evidenced by the correlation between ^3He and Li observed for pyroxenes (Fig. 3). To understand this ^3He component in relation to other components we use the following equation:

$$^3He_m = {}^3He_{sp} + {}^3He_{in} + {}^3He_{nuc} + {}^3He_{cn} + {}^3He_{mu} \quad (1)$$

where ^3He_m is the total ^3He measured in the sample, $^3He_{sp}$ is spallation-produced ^3He, $^3He_{in}$ is inherited from inclusions or prior exposure, $^3He_{nuc}$ is the Li-produced nucleogenic component produced by capture of radiogenic neutrons, $^3He_{cn}$ is the Li-produced component produced by capture of cosmogenically derived low energy neutrons, and $^3He_{mu}$ is the Li-produced component produced by stopping of muons or by capture of muogenic neutrons.

Table 4
Pyroxene helium results.

	n	^3He_m (Mat/g)	1σ (Mat/g)	^4He (Tat/g)	1σ (Tat/g)	$^3He/^4He$ (Ra)	Li (ppm)	$^3He_{nuc}$ (Mat/g)	$^3He_{sp+cn}$ (Mat/g)	$^3He_{cn}$ (Mat/g)	$1\sigma_{cn}$ (Mat/g)	$^3He_{sp}$ (Mat/g)	1σ (Mat/g)	^3He PR (at g^{-1} yr^{-1})	1σ (at g^{-1} yr^{-1})
"Reset" surfaces and shielded samples															
ID2	2	6.7	0.3	53	4	0.1	17	1.6	5.1	0.5	0.1	4.7	0.4	127	23
ID4	3	8.5	0.3	52	4	0.1	34	2.8	5.8	0.9	0.1	4.8	0.4	132	24
ID5	4	10.3	0.4	43	3	0.2	53	4.1	6.2	1.5	0.2	4.7	0.4	128	26
ID6	2	6.9	0.3	50	3	0.1	16	1.5	5.4	0.4	0.1	5.0	0.4	136	24
ID9	1	7.8	0.5	40	2	0.2	25	2.1	5.7	0.7	0.1	5.0	0.6	135	34
ID11	2	10.6	0.5	47	3	0.2	62	4.7	5.9	1.7	0.2	4.2	0.6	114	35
Weighted mean												***4.7***	***0.1***	***129***	***10***
ID8 (s)	8	6.9	0.2	53	5	0.0	90	7.4	–	–	–	–	–	–	–
ID13 (s)	7	4.3	0.1	72	8	0.0	57	4.6	–	–	–	–	–	–	–
"Unreset" surfaces															
ID10	2	31.6	1.6	49	2	0.5	17	1.6	30.0	3.3	0.4	26.7	1.6	–	–
ID12	2	37.4	1.9	79	2	0.4	17	1.6	35.9	4.1	0.5	31.7	1.9	–	–
ID14	2	15.8	0.8	57	3	0.2	20	1.8	14.0	1.8	0.2	12.3	0.8	–	–
ID16	1	28.7	2.0	84	2	0.3	20	1.8	27.0	3.8	0.5	23.1	2.1	–	–

n = # of replicate analyses; 1σ = standard error, MER = mean equivalent radius; $1\sigma_{cn}$ = Monte Carlo standard deviation on $^3He_{cn}$ component; ^3He_m = measured; $^3He_{cn}$ = modeled ^3He from ^6Li and cosmogenic neutrons; $^3He_{sp}$ = net spallation ^3He after subtraction of Li-produced components. Production rates are determined using a scaling factor of 2.1 and assumed age of 17,500 ± 500 yrs (1 σ) for Bonneville flood event.

Table 5
Crushing data.

	Mass (g)	^{3}He (Mat/g)	1σ (Mat/g)	^{4}He (Tat/g)	1σ (Tat/g)	^{3}He/^{4}He (Ra)	1σ (Ra)
Pyroxene (Lower Unit)							
ID4	90	0.02	0.05	0.27	0.03	0.06	0.11
ID8	75	0.05	0.07	0.93	0.03	0.04	0.04
ID11	102	0.09	0.05	0.44	0.03	0.14	0.06
Mean		***0.05***		***0.55***		***0.08***	
Pyroxene (Upper Unit)							
ID2	74	0.26	0.08	0.69	0.04	0.27	0.05
ID6	75	0.18	0.07	0.62	0.03	0.20	0.06
ID16	87	0.26	0.07	0.66	0.03	0.28	0.05
Mean		***0.23***		***0.66***		***0.25***	
Apatite							
ID13a*	12	0.19	0.42	6.66	0.22	0.02	0.03
ID13b*	10	0.05	0.46	7.29	0.26	0.01	0.04

*Not all grains were completely crushed.

The use of a shielded sample allows the $^3He_{nuc}$ component to be directly removed from this equation. Because the magmatic $^3He_{in}$ component has been removed by crushing and because we neglect the muon produced $^3He_{mu}$ component in these samples (see below), we assume that all of the ^{3}He measured in the shielded samples is Li-produced nucleogenic ^{3}He, and refer to it as "measured $^3He_{nuc}$". For pyroxene, we exploit the linear relationship between measured $^3He_{nuc}$ and Li content in shielded samples to directly subtract the $^3He_{nuc}$ component from the surface exposure samples, which also span a range of Li contents (Fig. 3). The sizes of the $^3He_{nuc}$ components for pyroxene range between ~1.5–4.7 Mat/g, or ~18–45% of the measured surface concentrations (Table 4). Because the shielded ^{3}He components are measured with an equal degree of precision to exposure samples, subtraction of the shielded component does not significantly increase the error. Apparent production rates of ~154 at $g^{-1}\,a^{-1}$ are thus obtained for pyroxene, which are higher than previously obtained values (Goehring et al., 2010) due to the presence of the $^3He_{cn}$ component (quantified below).

Similar corrections for the apatites and zircons must accommodate the fact that their average grain size is comparable to the stopping range of ^{6}Li-produced ^{3}H in common silicate minerals (~30 μm). As a result the redistribution of this component among the rock's constituent phases must be evaluated. Because their Li contents are lower than in the surrounding matrix, the net effect for apatites and zircons is implantation; the smaller the grain size, the more significant the effect (Farley et al., 2006; Dunai et al., 2007). This effect explains, for example, the increase of $^3He_{nuc}$ from ~0.8 Mat/g for MER = 105 μm to ~1.8 Mat/g for MER = 27 μm in the shielded zircons (Fig. 2). For these two phases we thus subtract the mean $^3He_{nuc}$ measured on shielded samples of a given grain size from all surface samples of that same grain size. This approach does not account for variations in Li concentration between different apatite and zircon samples, or variations in the average Li concentrations of their adjacent minerals. However, it is reasonable to ignore these effects because: 1) the mean concentration of Li in zircon is very low and relatively constant at ~1.5 ± 0.3 ppm, 2) the concentration of Li in apatite is higher and more variable (5 ± 2 ppm) but small grain sizes make internal Li concentration much less important than matrix Li, and 3) we have no independent means with which to evaluate differences in average host Li concentrations. The sample-to-sample consistency of our results at a given grain size validates this simplification. The resultant apparent production rates ($^3He_{sp} + {}^3He_{cn}$) are ~156 at $g^{-1}\,a^{-1}$ for apatite, and range from 108 to 136 at $g^{-1}\,a^{-1}$ for zircon of different grain sizes. Note that both $^3He_{sp}$ and $^3He_{cn}$ are also dependent on grain size as a consequence of redistribution, so this spread in zircon is expected.

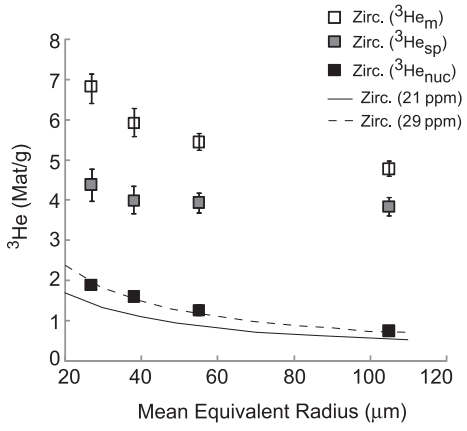

Fig. 2. Measured ^{3}He in shielded zircons (black squares), reset surfaces (open squares), and spallation-produced ^{3}He in reset surfaces (gray squares). All are plotted against mean equivalent radius. Solid and dashed lines show model calculation of the nucleogenic ^{3}He component assuming an average Li content of adjacent phases of 21 and 29 ppm respectively. These values equal the measured bulk rock concentration and the best fit to the data. Error bars denote 1σ standard errors.

5.2. Additional ^{3}He components

In previous work (Amidon et al., 2008, 2009), we outlined the model calculations necessary to predict each Li-produced ^{3}He component. The present dataset allows us to test these calculations by comparison of the ^{3}He concentrations in surface and shielded samples with measured Li concentrations. More importantly, the model also allows us to compute $^3He_{cn}$, so we can isolate the spallation production rate in these phases. The calculation procedures are only briefly discussed below, but are included as an Appendix to this paper. For comparison with past and future models, the inputs and resultant neutron flux parameters are tabulated in Online Tables 3 and 4.

The low-energy neutrons that drive ^{3}He production from ^{6}Li are derived from three primary sources: 1) radiogenic neutrons produced by decay of U and Th whose alpha particles are involved in (α,n) reactions on light elements (Andrews and Kay, 1982; Chmiel et al., 2003), 2) 'tertiary' cosmogenic neutrons produced by excitation of target nuclei in rock by high-energy atmospheric neutrons (Phillips et al., 2001; Dunai et al., 2007), and 3) muogenic neutrons produced by slowing and stopping of muons by target nuclei in rock (Heisinger et al., 2002a,b). Before any neutrons have a high probability of being captured by ^{6}Li, they need to be slowed down (thermalized) by elastic collisions with other nuclei in the rock. Because smaller nuclei can absorb more kinetic energy during a collision, the low-energy neutron flux is very sensitive to hydrogen (i.e. water) content in the rock. The low-energy neutron flux is also limited by the total ability of nuclei in the rock to absorb (capture) neutrons. Because some elements have very large neutron capture cross-sections (Li, B, Gd, etc.), the neutron flux is a sensitive function of the bulk rock concentration of these elements. The compositions and other constants used in our calculations are given in Online Table 4.

For a given low-energy neutron flux, ^{3}H production via neutron capture is proportional to Li concentration. Because ^{3}H produced via the ^{6}Li(n,α)^{3}H reaction has a stopping range of ~30 μm in common minerals, significant redistribution can occur between adjacent mineral phases (Ziegler, 2003; Farley et al., 2006). This

Table 6
Li, U, and Th concentrations (ppm).

	Li							U				Th			
	Px	Zr	Ap	G.M.	W.R.	FeO	Plag.	Px	Zr	G.M.	W.R.	Px	Zr	G.M.	W.R.
ID1	–	2	–	–	–	–	–	–	249	–	–	–	–	–	–
ID2	17	2	4	–	–	–	–	–	243	–	–	–	104	–	–
ID4	34	2	7	–	–	–	–	–	205	–	–	0.3	121	–	–
ID5	53	2	–	42	22	33	–	0.1	270	8	–	0.2	169	21	–
ID6	16	1	3	11	–	11	10	0.1	–	–	–	0.3	–	–	–
ID8	90	2	8	8	19	–	30	0.3	459	–	–	1.0	436	–	–
ID9	25	2	–	11	15	–	17	–	200	–	7	–	109	–	17
ID10	–	–	–	–	–	–	–	–	270	–	–	–	109	–	–
ID11	67	2	–	9	22	–	–	0.1	290	8	6	0.4	204	23	14
ID12	17	1	4	4	17	–	–	0.1	236	9	7	0.4	129	23	18
ID13	53	2	6	14	22	–	33	0.1	238	–	–	0.2	137	–	–
ID14	–	–	3	–	–	–	–	–	–	–	–	–	–	–	–
ID16	20	1	–	3	15	–	–	0.1	219	9	7	0.3	120	22	19

G.M. = handpicked groundmass fragments; W.R. = powdered whole rock.

redistribution is quantitatively modeled by determining the mean equivalent spherical radius of sample grains, and using the equation for implant and export of ions from a sphere (Farley et al., 1996, 2006; Dunai and Wijbrans, 2000).

5.2.1. Inherited component ($^3He_{in}$)

The inherited component can be derived either from trapped magmatic helium or from prior exposure of the sample. Crushing experiments show that the trapped magmatic component amounts to <2% of the measured ^{3}He in our samples. This small amount of helium should largely be removed from pyroxene by crushing prior to fusion. Apatite and zircon were not crushed prior to analysis because they are unlikely to have significant trapped components in their tiny grains and because any magmatic ^{3}He is included in our corrections based on the shielded samples. Regarding prior exposure, consistent ^{3}He concentrations in our reset samples suggests that >3 m of rock was removed during the Bonneville flood and that the samples do not contain a $^3He_{in}$ component.

5.2.2. Nucleogenic component ($^3He_{nuc}$)

Our fluence calculations described in the Appendix are very close to, but slightly overestimate, the measured concentration of ^{3}He in shielded pyroxene (see $^3He_{nuc}$ for samples ID8 and ID13 in Table 4). Although the ~6% discrepancy is within error of the calculation inputs, it is worth considering possible explanations such as: 1) an erroneously old crystallization age, 2) underestimates of neutron absorbers or overestimates of U or Th concentrations, or 3) a violation of the assumption that all elements are evenly distributed throughout the rock. The third possibility is likely if the alpha-emitters (U and Th) are isolated in different mineral phases than elements with high (α,n) cross-sections (Na, Al, and Si), thereby preventing (α,n) reactions due to the short (~20 μm) range of α particles. The last point has been raised by several previous authors, and is worthy of a brief discussion here (Martel et al., 1990; Ballentine and Burnard, 2002; Hu et al., 2009).

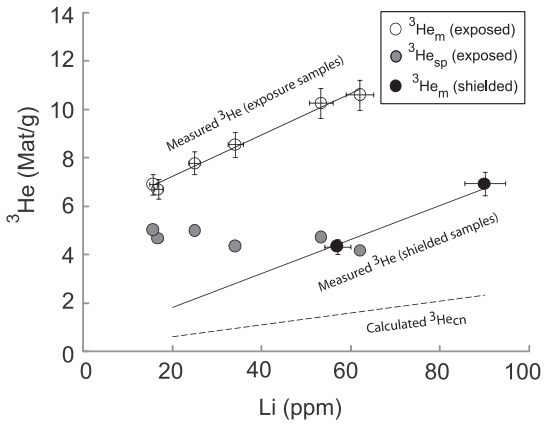

Fig. 3. Plot of ^{3}He vs Li content for pyroxene grains of >190 μm grain size. Open symbols are measured ^{3}He in the reset samples. Gray symbols denote spallation-produced ^{3}He in the same samples after subtraction of all Li-produced components. Black circles denote measured nucleogenic ^{3}He ($^3He_{nuc}$) in the two shielded samples. Solid lines are linear regressions through data, dashed line shows the calculated $^3He_{cn}$ component as a function of Li concentration.

Two simple arguments suggest that the homogeneity assumption is valid in the present case. First, the concentration of U and Th in the groundmass is higher than in the bulk rock by approximately its fractional abundance estimated from point counting, suggesting that virtually all of the U and Th is contained in the groundmass. Second, mineral compositions and point counting show that almost all of the Na and Al (which account for ~60% of (α,n) reactions) are contained in the groundmass and that Si and O (which account for the rest) are evenly distributed throughout the rock. Because almost all of the U, Th, Na and Al is contained in the groundmass, the homogeneity assumption appears to be valid for these rhyolites. However in general this may not be true; rocks in which a large fraction of U,Th is housed in trace phases poor in light elements (zircon, monazite, xenotime, etc) will have less nucleogenic ^{3}He than our model would estimate. Importantly, if U and Th are concentrated in accessory phases, the grain sizes need only be larger than ~25 μm to create an inhomogenous distribution of alpha-emitters.

Shielded zircon and apatite crystals of a range of (small) grain sizes allow us to estimate the average Li content of adjacent phases. This is useful because the Li content of adjacent phases is required for the calculation of the $^3He_{cn}$ component for exposed samples. The plot of $^3He_{nuc}$ vs grain size shows a strong grain size dependence in shielded zircon, implying that the average Li content of adjacent minerals is higher than the internal Li content (Fig. 2). For both mineral phases, we initially assumed that the average host Li content was equal to the bulk rock Li concentration (~21 ppm). As shown by the solid line in Fig. 2, this led to significant underestimates for both zircon and apatite (not shown). This underestimate is consistent with previous studies in which the average host Li concentration (computed by point counting) was higher than the bulk rock due to the presence of high Li phases such as biotite (or groundmass) preferentially in contact with apatite and zircon (Amidon et al., 2009). The best fit (least-squares) agreement between observed and modeled data is achieved with a host Li concentration of 29 ppm for zircon and 46 ppm for apatite.

5.2.3. Cosmogenic neutron and muogenic components ($^3He_{cn}$ and $^3He_{mu}$)

Although muogenic production has been explicitly considered in previous studies, it is thought to produce ≪1% of the measured ^{3}He in all phases and is thus not considered further (Lal, 1987; Amidon et al., 2009). The cosmogenic neutron ($^3He_{cn}$) component is produced only when the sample is exposed within ~3 m of the surface. Because it is convolved with the spallogenic component, we have no independent observations (such as shielded samples) with which to assess its magnitude and must therefore rely on calculated values (see Appendix for details). For reset surfaces $^3He_{cn}$ is determined by multiplying the modeled $^3He_{cn}$ production rate (1.57 at $g^{-1}\,a^{-1}$ ppm Li^{-1}) by the known exposure age of 17.5 ka (Online Table 3). For unreset surfaces we capitalize on the fact that following subtraction of the nucleogenic component, all remaining ^{3}He can be attributed to the $^3He_{cn}$ and $^3He_{sp}$ components (i.e. $^3He_{sp+cn}$ in Tables 1–3). We then use the newly determined local spallogenic production rate in pyroxene (270 at $g^{-1}\,a^{-1}$) to solve for the apparent exposure age (time) and the $^3He_{cn}$ component using the relationship: $\text{time} = (^3He_{sp+}{}^3He_{cn})/(p^3He_{sp} + p^3He_{cn})$. The exposure ages determined using the pyroxene data are then used to solve for $^3He_{cn}$ in zircon and apatite. Due to the relatively young exposure ages considered in this study, the $^3He_{cn}$ components are small; ~0.3 Mat/g for zircon, ~0.8 Mat/g for apatite, and ~1 Mat/g for pyroxene where the variability reflects differences in effective Li concentration. The largest uncertainties in calculating $^3He_{cn}$ arise from the neutron fluence computation and the average Li content of adjacent minerals (see above).

5.3. Uncertainty of $^3He_{sp}$ estimates

Several lines of evidence suggest that we have accurately isolated the $^3He_{sp}$ components listed in Tables 2–4. First, the slope of the Li vs $^3He_{sp}$ line for pyroxene is within error of zero, implying no under- or overcorrection for Li-produced components (Fig. 3). Second, when $^3He_{sp}$ concentrations in pyroxene are plotted against $^3He_{sp}$ in zircon (all >50 μm fractions), an excellent linear fit of $[^3He_{sp(zr)}] = 0.77 * [^3He_{sp(px)}] + 0.02$ is obtained for units of Mat/g (Fig. 4). The intercept of this line is within error of zero suggesting that the spallation-induced component has been correctly isolated in both phases. In contrast, a plot of $^3He_{sp}$ concentrations in apatite against pyroxene yields a linear fit that does not pass through the origin, and has a shallower slope than the zircon-pyroxene plot (Fig. 4). Based on previous results, apatite should have a steeper slope (i.e. higher production rate) relative to pyroxene than does zircon (Farley et al., 2006; Amidon et al., 2008, 2009). Because the reset samples give sensible ^{3}He concentrations and production rates in relation to zircon and apatite, it appears that this shallow slope and high intercept may be due to leverage on the line exerted by erroneously low $^3He_{sp}$ concentrations in the three unreset samples (12, 14 and 16). The measured ^{3}He concentrations in apatite from these samples are 20–35% lower than expected based on measurements in zircon and pyroxene, a larger deficit than the entirety of the $^3He_{cn}$ correction in these samples. Because the apparent deficit is so large, it is difficult to attribute to the incorrect calculation of any of the Li-produced ^{3}He components. We lack a satisfactory explanation for this observation.

The uncertainties on our final $^3He_{sp}$ concentrations combine analytical errors with the uncertainty on calculation of the Li-produced components (Tables 1–3). The standard error for each sample (shielded or exposed) is determined by dividing the combined weighted analytical uncertainty by the square root of n replicate analyses. Uncertainties on the Li-produced $^3He_{cn}$ component were calculated using a Monte-Carlo simulation in which 8 variables were allowed to vary over 1000 trials. These variables include internal Li content of the mineral (1σ = 8%), average Li content of adjacent minerals (1σ = 15%), bulk rock concentrations of the trace elements that strongly modulate neutron production or absorption (H, Li, B, Gd, and Sm) (1σ = 12%), and grain radius (1σ = 5%). Depending on grain size, these input errors result in 13–18% standard deviation on the total Li-produced ^{3}He.

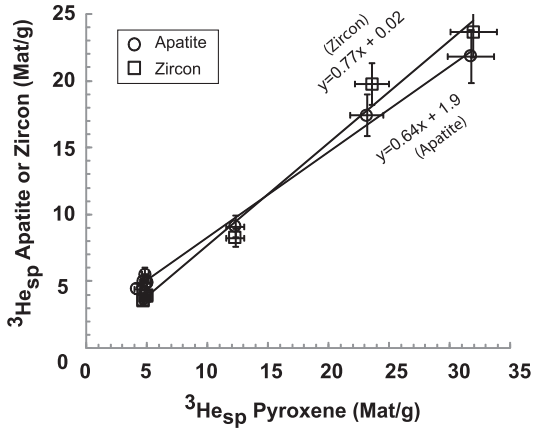

Fig. 4. Plot of spallation-produced ^{3}He in pyroxene against both apatite (circles) and zircon (squares). Regression lines and equations are indicated. Note that the zircon regression line passes through the origin, as expected. In contrast the shallow slope and the non-zero intercept for the apatites are unexpected and suggest anomalously low ^{3}He concentrations in the unreset samples.

To determine the 1σ error on the $^3He_{sp}$ component for a given grain size, we first compute the weighted standard error on $^3He_{sp}$ for all of the reset surface exposure samples of that grain size. This uncertainty is then added in quadrature with the uncertainties on the $^3He_{nuc}$ and $^3He_{cn}$ components, which are taken as the standard deviation of ^3He_m for the shielded sample and the Monte-Carlo standard deviation on the calculated $^3He_{cn}$ component for that grain size. For zircon, because the production rates for the three largest grain size categories are within error of each other, the grand mean $^3He_{sp}$ is computed as the weighted mean of the three. The standard deviation of the grand mean is then propagated with the 1σ error on the age of the Bonneville outburst flood (±0.5 ka) to compute a 1σ uncertainty on the final production rate estimate for each mineral phase.

6. Discussion

6.1. Production rates of spallogenic ^{3}He

This study provides the fourth calibration of production rates in zircon and apatite (Farley et al., 2006; Amidon et al., 2008, 2009). Because the three previous studies have calibrated against ^{10}Be and/or ^{21}Ne, their published production rates are dependent upon the accepted production rates of ^{10}Be and ^{21}Ne in quartz. As a consequence, Table 7 summarizes published $^3He/^{10}Be_{qtz}$ ratios from previous studies and reports revised production rates relative to an SLHL $^{10}Be_{qtz}$ production rate of 4.51 at $g^{-1}\,a^{-1}$ (including muogenic production). This revised value for the $^{10}Be_{qtz}$ production rate comes from a weighted average of the five production rate scaling schemes presented in Balco et al. (2008), adjusted by a factor of 0.904 to reflect the revised $^{10}Be/^9$Be ratio of the 07KNSTD3110 standard (Niishizumi et al., 2007; Balco et al., 2008). Although there is no statistical basis for averaging production rates derived from different scaling models it is done here to obtain reference production rates that simplify the discussion.

Table 7
Summary of previous ^{3}He production rate calibrations in accessory mineral phases (at $g^{-1}\,a^{-1}$).

	Idaho (This Study)					Coso (Amidon et al., 2009)			Nepal# (Amidon et al., 2008)			Bolivia (Farley et al., 2006)			
	St	De	Du	Li	**Avg.**	$^3He/^{10}Be_{qtz}$	**Pub**	*Rev.*	$^3He/^{10}Be^{\#}_{qtz}$	**Pub**	*Rev.*	$^3He/^{21}Ne_{qtz}$	$^3He/^{10}Be_{qtz}$	**Pub**	*Rev.*
$^{10}Be_{qtz}$ P.R.	–	–	–	–	–	–	**4.87**	*4.51*	–	**4.98**	*4.51*	–	–	**4.87**	*4.51*
p^{3}He Zirc.	96	106	106	113	**105**	23.3	**114**	*105*	30.4	**135**	*137*	3.9	22.1	**87**	*100*
p^{3}He Ap.	123	136	136	146	**135**	30.6	**149**	*138*	37.7	**168**	*170*	5.0	28.0	**112**	*126*
p^{3}He Px.	117	130	130	139	**129**	29.7	**145**	*134*		–	–	–	–	–	–
p^{3}He Gnt.	–	–	–	–	–	29.7	**144**	*134*	34.0	**153**	*153*	–	–	–	–
p^{3}He Tit.	–	–	–	–	–	–	–	–		–	–	4.3	24.5	**97**	*110*
p^{3}He Ky.	–	–	–	–	–	–	–	–	39.6	**177**	*179*	–	–	–	–

"Pub" denotes previously published values; *"Rev"* denotes values recalculated using average $^{10}Be_{qtz}$ production rates from Balco et al. (2008). # denotes that only the lowest elevation sample (CRN 259) are reported here. ^{10}Be values revised relative to 07KNSTD3110 $^{10}Be/^9Be$ ratio. "St", "De", "Du", and "Li" denote different scaling schemes (2.3, 2.08, 2.08, 1.94) following the notation introduced in Balco et al. (2008).

One of the motivations of this study is to produce a set of production rate estimates for zircon and apatite that are independent of the ^{10}Be production rate. We obtain production rates of $\sim 105 \pm 9$ and $\sim 135 \pm 17$ at $g^{-1}\,a^{-1}$ for zircon and apatite averaged over the four scaling models in Table 7. These rates agree well with the revised rates of ~ 103 and ~ 132 at $g^{-1}\,a^{-1}$ obtained by calibrating ^{3}He against ^{10}Be in quartz ($p^{10}Be_{qtz} = 4.51$ at $g^{-1}\,a^{-1}$) from rhyolite surfaces in Bolivia and California (Amidon et al., 2009). It is important to emphasize that zircon production rates reflect mean values for grain sizes of MER ≥ 38 μm, and may not apply to smaller grain sizes due to redistribution of spalled ^{3}He and ^{3}H from adjacent mineral phases. In contrast, apatite production rates likely apply to a full range of grain sizes because ^{3}H and ^{3}He production rates in adjacent silicate minerals should be comparable to those in apatite (Farley et al., 2006).

For pyroxene, we calculate a production rate of 129 ± 10 at $g^{-1}\,a^{-1}$ averaged over the four scaling models in Table 7, which also lists scaling factors and production rates calculated using each individual scaling model. These values are within the range of six previous studies, and agree very well with the range of 120–136 at $g^{-1}\,a^{-1}$ recently recalculated against ^{14}C for the nearby Tabernacle Hill site (Goehring et al., 2010). These rates are also in agreement with the revised rate of 134 at $g^{-1}\,a^{-1}$ for pyroxene determined against ^{10}Be in quartz ($p^{10}Be_{qtz} = 4.51$ at $g^{-1}\,a^{-1}$) at Coso, California (Amidon et al., 2009).

Based on several recent studies, it seems likely that the ^{10}Be production rate of 4.51 at $g^{-1}\,a^{-1}$ may not be a globally applicable value (Balco et al., 2009; Putnam et al., 2010). We therefore express the zircon and apatite production rates as the arithmetic mean of results from three existing studies, two of which are dependent on the SLHL ^{10}Be production rate in quartz ($p^{10}Be_{qtz}$).

$$\frac{P^3He_{zirc} = (105 + 23.3{*}P^{10}Be_{qtz} + 22.1{*}P^{10}Be_{qtz})}{3} \quad (2)$$

$$\frac{P^3He_{ap} = (135 + 30.6{*}P^{10}Be_{qtz} + 28{*}P^{10}Be_{qtz})}{3} \quad (3)$$

We have not included estimates from the Nepal study of Amidon et al. (2008) in these equations because they are clear outliers from the three other datasets in Table 7. These samples were measured at elevations of 3200–4600 m near the maximum in rigidity cutoff. Further studies at high elevations and high rigidity cutoff are required to determine if ^{3}He and/or ^{10}Be production rates are sensitive to changes in the energy spectrum of incident nucleons at these locations. In any case all recent work confirms the peculiarity of ^{3}He production rate studies in the Himalaya (Gayer et al., 2004; Amidon et al., 2008) and justifies their exclusion from this computation.

When a value of 4.51 at $g^{-1}\,a^{-1}$ is used, the standard deviation of the three zircon production rates is reduced from 14 to 3 at $g^{-1}\,a^{-1}$, and for apatite from 18 down to 6 at $g^{-1}\,a^{-1}$. The grand mean production rates for spallation-produced ^{3}He are 103 ± 3 at $g^{-1}\,a^{-1}$ for zircon (MER ≥ 38 μm) and 133 ± 6 at $g^{-1}\,a^{-1}$ for apatite.

6.2. Criteria for ^{3}He dating with zircon and apatite

The new data presented in this study, and their agreement with revised production rates from previous studies (Table 7) strongly suggest that zircon and apatite can be successfully used for cosmogenic ^{3}He dating, at least under certain circumstances. The most fundamental limitation on the technique is the size of the spallation-produced ^{3}He component ($^3He_{sp}$) relative to the Li-produced ^{3}He components ($^3He_{nuc}$, $^3He_{cn}$, $^3He_{mu}$). Whereas the size of the $^3He_{sp}$ component is entirely a function of location and exposure age, the Li-produced components additionally depend on the Li content, closure age, and to a lesser extent, grain size. Because the Li content of neighboring minerals is typically much higher than in zircon or apatite, the size of the Li-produced component can be reduced by working with large grains (MER ≥ 38 μm), that are less vulnerable to implantation. A useful metric with which to quantify the vulnerability of a given sample to Li-produced ^{3}He is the apparent Li (Li_a). This is calculated using the implant/export equation, which includes the internal Li content (Li_i), the average Li content of adjacent "host" minerals (Li_h), MER (R), and the range of Li-produced ^{3}H in common silicate minerals (S):

$$Li_a = Li_i\left[1 - 0.75\left(\frac{S}{R}\right) + 0.0625\left(\frac{S}{R}\right)^3\right] + Li_h\left[0.75\left(\frac{S}{R}\right) - 0.0625\left(\frac{S}{R}\right)^3\right] \quad (4)$$

For example, a zircon with MER = 50 μm, internal Li = 2 ppm, and host Li = 20 ppm would have an apparent Li of ~ 10 ppm.

For a given apparent Li concentration the ratio of $^3He_{sp}/^3He_{tot}$ is a function of exposure age and the He closure age of the specific mineral analyzed. The He closure age is identical to the (U–Th)/He age and varies among mineral phases depending upon He diffusion characteristics. Thus, for rocks that have been exhumed from great depths and high temperatures, minerals with higher He diffusivity (e.g., apatite) will have a lower nucleogenic ^{3}He content than minerals with low diffusivity (e.g., zircon) (Wolf et al., 1996; Reiners et al., 2002). Fig. 5 shows the evolution of the $^3He_{sp}/^3He_{tot}$ ratio as a function of exposure age, closure age and apparent Li content. As a practical example of how this figure can be used, limiting the Li-produced ^{3}He component to $\sim 50\%$ of the total for an apparent Li content of 10 ppm and a ~ 10 My closure age would require

a ~7 ka exposure at 1000 m elevation. This limitation is relaxed at higher elevations as the spallation production rate increases. Based on our limited survey data (Amidon and Farley, unpublished), zircons and apatites of large grain size in continental igneous rocks have apparent Li concentrations ranging from 5 to 20 ppm.

If Li-produced components are large compared to spallation ^{3}He, they limit the accuracy with which the surface exposure age can be determined. The three primary sources of error are the analytical errors on the exposed and shielded samples, and the error on the model calculation of the $^3He_{cn}$ component. Because analytical errors are directly related to the concentration of ^{3}He in the sample they become relatively smaller for samples with older exposure ages (or more nucleogenic ^{3}He in the shielded case). In contrast, because the error on the calculated $^3He_{cn}$ component is primarily a function of how well the composition of the rock and the Li content is known, its contribution to the total error increases with Li content.

In many cases, even Li-rich samples can provide relatively precise exposure age estimates. For example, in this study we measure a concentration $\sim 10.3 \pm 0.4$ (~4%) Mat/g of ^{3}He in an exposed pyroxene sample, and 4.1 ± 0.1 (~3%) in a shielded pyroxene with a similar Li concentration (~57 ppm). Because it is determined with reasonable precision, subtracting the $^3He_{nuc}$ component gives $\sim 6.2 \pm 0.4$, only moderately increasing the error (to ~7%). The relative error on the modeled $^3He_{cn}$ component is large at $\sim 1.5 \pm 0.2$ (~13%), but its small absolute value means that it contributes relatively little to the final error of 4.7 ± 0.4 (~9%) on its $^3He_{sp}$. Fig. 6 illustrates approximately how these different sources of error propagate in samples of different exposure age, closure age, and apparent Li content. As an example of its use, we have plotted a hypothetical sample from a ~18 ka Tioga-aged moraine boulder exposed at ~2250 m elevation in the Sierra Nevada mountains of California. Assuming an apparent Li of 10 ppm and a (U/Th)-He closure age of 50 Ma, the $^3He_{sp}$ component in apatite could be determined with a precision of ~7% (circle in Fig. 6). This assumes a single analysis of a 30 mg aliquot of material, and the use of a shielded sample to make the correction for $^3He_{nuc}$.

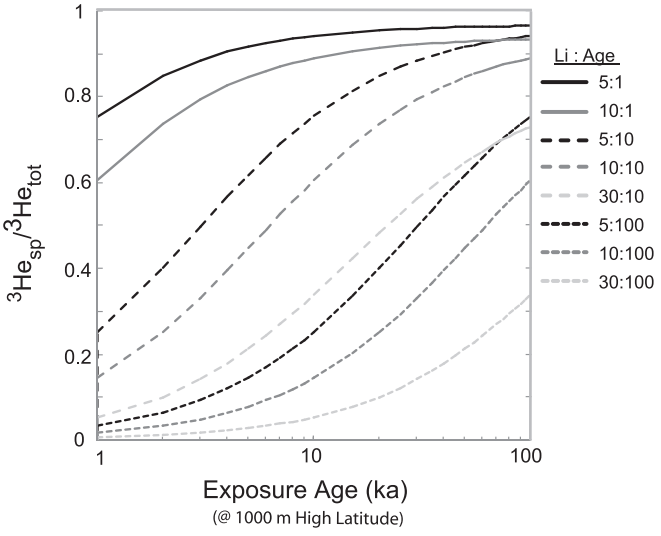

Fig. 5. Calculations showing the fraction of spallation-produced ^{3}He in apatite as a function of the He closure age, apparent Li content, and exposure age at a 1000 m elevation, high-latitude site. Apparent Li is in units of ppm and closure age is in units of Ma. Calculations assume a typical granitic composition with 12 ppm of Th and 4 ppm of U. Spallation-produced fractions will increase for higher elevation samples and decrease for lower elevations.

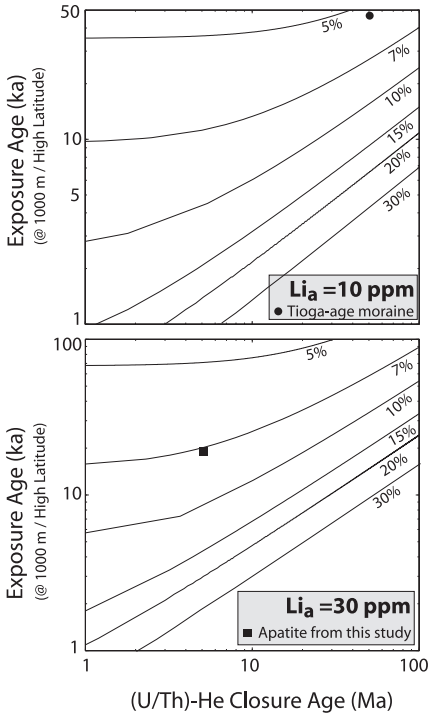

Fig. 6. Calculations showing the 1σ uncertainties with which the $^3He_{sp}$ component can be determined in apatite from a sample collected at a 1000 m elevation, high-latitude site. Symbols show typical samples from this study, and from a Tioga-aged moraine composed of a typical Sierra Nevada granodiorite. Although the Tioga age moraine is ~18 ka, it has been plotted at an age of ~50 ka to reflect higher production rates near the occurrence of these moraines at elevations of ~2500 m rather than the 1000 m for which the lines of constant error are plotted. This calculation assumes typical measurement sensitivities obtained at Caltech, and a single analysis of ~30 mg of apatite from the >75 μm size fraction. This quantity of apatite can routinely be obtained from ~1 kg of granitoid rock.

6.3. Geomorphic implications

In addition to providing an opportunity for calibration of ^{3}He production rates, our data also provide insight into the incision history of the Snake River canyon. The most fundamental observation is that all samples from the upstream site (Pillar Falls) experienced greater than ~3 m of bedrock erosion during the Bonneville flood whereas most samples from the wider part of the canyon below Perrine bridge experienced incomplete erosional resetting. Notably, two of the unreset samples below Perrine bridge (10 and 12) are closer to the modern river level than any of the upstream samples. The apparent contrast between the intensity of erosion at Pillar Falls and further downstream is surprising given that many models of fluvial erosion assume that shear stress on the river bed is proportional to water depth, and thus predict that the wide and narrow parts of the canyon should experience similar erosive forces as long as they are both bank full (Rosgen, 1994).

Based on the observations above, it seems that the depth and width of the canyon below Perrine bridge were not significantly altered by the Bonneville outburst flood. Although our data are insufficient to precisely constrain this earlier history, it seems plausible that much of the existing canyon, including the extensive fluted and potholed bedrock surfaces below Perrine Bridge (samples 14 and 16), may have formed during previous flood events. Such a flood event would have formed much of the surface as it exists today, followed by a minor amount of erosion during the Bonneville flood to create the well-preserved scour features. This idea is intriguing because neither the Eden/Rupert overland channel nor the scoured alcoves have been directly dated to

Bonneville age. Additionally, recent work in the Hagerman area has shown that Box canyon, a similar feature to the Blue Lakes alcove, likely formed during pre-Bonneville flood events (Lamb et al., 2008). Finally, the apparent exposure ages of samples 10, 12 and 16 (89, 110, and 89 ka) are similar to the 92 ka average age of three paleo-flood surfaces documented along the Big Lost River, a tributary to the Snake River (Cerling et al., 1994). Future work should focus on dating erosional features along the Eden overflow channel to directly tie them to the Bonneville flood, or alternatively, tie them to possible earlier flood events.

7. Conclusions

New cosmogenic ^{3}He measurements in zircon, apatite and pyroxene from eight scoured rhyolite surfaces thought to be the product of the Bonneville outburst flood fall into one of two classes. The first class of samples yielded ^{3}He concentrations that are within error of each other. When corrected for non-spallation ^{3}He using shielded samples and a model for $^{3}He_{cn}$ production, these samples can be used to calibrate the spallation production rate of ^{3}He against the known ^{14}C age of the Bonneville outburst flood. Synthesizing these new results with previous calibration studies performed by reference to ^{10}Be shows that the ^{3}He production rates in apatite and zircon agree to within 5% if an averaged ^{10}Be production rate of 4.51 at $g^{-1}\,a^{-1}$ is adopted (Balco et al., 2008). Making this assumption we obtain a best estimate for the SLHL production rate of 103 ± 3 at $g^{-1}\,a^{-1}$ for zircon (MER $>= 38$ μm) and 133 ± 6 at $g^{-1}\,a^{-1}$ for apatite. The second class of samples contains inherited ^{3}He from prior exposure, reflecting the complex incision history of the Snake River canyon and suggesting one or more earlier flood events.

These data suggest that uncertainties in production rate are no longer the major source of uncertainty in using spallation ^{3}He in apatite and zircon for surface exposure dating. Instead the biggest consideration is correction for ^{3}He produced from the capture of both nucleogenic and cosmogenic neutrons by ^{6}Li. We demonstrate that although Li-produced components can become large even in fairly young rocks ($>\sim$1 My), in many cases they can be reliably determined using shielded samples. Because zircons contain $\sim$10 times less Li than pyroxene and thus much smaller Li-produced components, they can provide more accurate age determinations in some cases.

Acknowledgments

We acknowledge funding from NSF grant EAR-0921295 as well as field assistance from Kevin Uno and insightful discussions with Michael Lamb. Careful reviews by Pete Burnard and Samuel Niedermann greatly improved the manuscript.

Appendix A. Supplementary information

Supplementary data associated with this article can be found, in the online version, at doi:10.1016/j.quageo.2010.03.005.

Editorial handling by: D. Bourlès

References

Ackert, R.P., Singer, B.S., Guillou, H., Kaplan, M.R., Kurz, M.D., 2003. Long-term cosmogenic ^{3}He production rates from ^{40}Ar/^{39}Ar and K–Ar dated Patagonian lava flows at 47 degrees S. Earth and Planetary Science Letters 210, 119–136.

Amidon, W., Farley, K.A., Burbank, D.W., Pratt-Sitaula, B., 2008. Anomalous cosmogenic ^{3}He production and elevation scaling in the high Himalaya. Earth and Planetary Science Letters 265, 287–301.

Amidon, W.H., Rood, D.H., Farley, K.A., 2009. Cosmogenic ^{3}He and ^{21}Ne production rates calibrated against ^{10}Be in minerals from the Coso volcanic field. Earth and Planetary Science Letters 280, 194–204.

Andrews, J.N., Kay, R.L.F., 1982. Natural production of tritium in permeable rocks. Nature 298, 361–363.

Armstrong, R.L., Leeman, W.P., Malde, H.E., 1975. K–Ar dating, Quaternary and Neogene volcanic-rocks of Snake River Plain, Idaho. American Journal of Science 275, 225–251.

Balco, G., Briner, J., Finkel, R.C., Rayburn, J.A., Ridge, J.C., Schaefer, J.M., 2009. Regional ^{10}Be production rate calibration for late-glacial northeastern North America. Quaternary Geochronology 4, 93–107.

Balco, G., Stone, J.O., Lifton, N.A., Dunai, T.J., 2008. A simple, internally consistent, and easily accessible means of calculating surface exposure ages or erosion rates from ^{10}Be and ^{26}Al measurements. Quaternary Geochronology 3, 174–195.

Ballentine, C.J., Burnard, P.G., 2002. Production, release and transport of noble gases in the continental crust. In: Porcelli, D., Ballentine, C.J., Wieler, R. (Eds.), Noble Gases in Geochemistry and Cosmochemistry, pp. 481–538.

Bierman, P., Steig, E.J., 1996. Estimating rates of denudation using cosmogenic isotope abundances in sediment. Earth Surface Processes and Landforms 21, 125–139.

Bierman, P.R., Gillespie, A.R., Caffee, M.W., 1995. Cosmogenic ages for earthquake recurrence intervals and debris flow fan deposition, Owens-Valley, California. Science 270, 447–450.

Blard, P.H., Pik, R., Lave, J., Bourles, D., Burnard, P.G., Yokochi, R., Marty, B., Trusdell, F., 2006. Cosmogenic ^{3}He production rates revisited from evidence of grain size dependent release of matrix-sited helium. Earth and Planetary Science Letters 247, 222–234.

Bonnichsen, B., Leeman, W.P., Honjo, N., McIntosh, W.C., Godchaux, M.M., 2008. Miocene silicic volcanism in southwestern Idaho: geochronology, geochemistry, and evolution of the central Snake River Plain. Bulletin of Volcanology 70, 315–342.

Brook, E.J., Kurz, M.D., Ackert, R.P., Denton, G.H., Brown, E.T., Raisbeck, G.M., Yiou, F., 1993. Chronology of Taylor Glacier Advances in Arena Valley, Antarctica, Using Insitu Cosmogenic ^{3}He and ^{10}Be. Quaternary Research 39, 11–23.

Cerling, T., 1990. Dating geomorphic surfaces using cosmogenic ^{3}He. Quaternary Research 33, 148–156.

Cerling, T., Craig, H., 1994. Cosmogenic ^{3}He production rates from 39N to 46N latitude, western USA and France. Geochimica et Cosmochimica Acta 58, 249–255.

Cerling, T.E., Poreda, R.J., Rathburn, S.L., 1994. Cosmogenic ^{3}He and ^{21}Ne Age of the Big Lost River Flood, Snake River Plain, Idaho. Geology 22, 227–230.

Chmiel, G., Fritz, S., Elmore, D., 2003. Control of ^{36}Cl production in carbonaceous shales by phosphate minerals. Geochimica et Cosmochimica Acta 13, 2377–2395.

Dunai, T., Stuart, F.M., Pik, R., Burnard, P.G., Gayer, E., 2007. Production of ^{3}He in crustal rocks by cosmogenic thermal neutrons. Earth and Planetary Science Letters 258, 228–236.

Dunai, T., Wijbrans, J., 2000. Long-term cosmogenic ^{3}He production rates (152 ka–1.35 Ma) from ^{40}Ar/^{39}Ar dated basalt flows at 29 N latitude. Earth and Planetary Science Letters 176, 147–156.

Farley, K.A., Libarkin, J., Mukhopadhyay, S., Amidon, W.H., 2006. Cosmogenic and nucleogenic ^{3}He in apatite, titanite, and zircon. Earth and Planetary Science Letters 248, 451–461.

Farley, K.A., Wolf, R.A., Silver, L.T., 1996. The effects of long alpha-stopping distances on (U–Th)/He ages. Geochimica Et Cosmochimica Acta 60, 4223–4229.

Gayer, E., Pik, R., Lave, J., France-Lanord, C., Bourles, D., Marty, B., 2004. Cosmogenic ^{3}He in Himalayan garnets indicating an altitude dependence of the ^{3}He/^{10}Be production ratio. Earth and Planetary Science Letters 229, 91–101.

Godsey, H.S., Currey, D.R., Chan, M.A., 2005. New evidence for an extended occupation of the Provo shoreline and implications for regional climate change, Pleistocene Lake Bonneville, Utah, USA. Quaternary Research 63, 212–223.

Goehring, B., Kurz, M., Balco, G., Schaefer, J., Licciardi, J., Lifton, N., 2010. A reevaluation of in situ cosmogenic ^{3}He production rates. Quaternary Geochronology 5 (4), 410–418.

Goethals, M.M., Hetzel, R., Niedermann, S., Wittmann, H., Fenton, C.R., Kubik, P.W., Christl, M., von Blanckenburg, F., 2009. An improved experimental determination of cosmogenic ^{10}Be/^{21}Ne and ^{26}Al/^{21}Ne production ratios in quartz. Earth and Planetary Science Letters 284, 187–198.

Handwerger, D.A., Cerling, T.E., Bruhn, R.L., 1999. Cosmogenic ^{14}C in carbonate rocks. Geomorphology 27, 13–24.

Heimsath, A.M., Dietrich, W.E., Nishiizumi, K., Finkel, R.C., 1997. The soil production function and landscape equilibrium. Nature 388, 358–361.

Heisinger, B., Lal, D., Jull, A.J.T., Kubik, P.W., Ivy-Ochs, S., Knie, K., Nolte, E., 2002a. Production of selected cosmogenic radionuclides by muons: 2. Capture of negative muons. Earth and Planetary Science Letters 200, 357–369.

Heisinger, B., Lal, D., Jull, A.J.T., Kubik, P.W., Ivy-Ochs, S., Neumaier, S., Knie, K., Lazarev, V., Nolte, E., 2002b. Production of selected cosmogenic radionuclides by muons: 1. fast muons. Earth and Planetary Science Letters 200, 345–355.

House, M.A., Farley, K.A., Stockli, D., 2000. Helium chronometry of apatite and titanite using Nd-YAG laser heating. Earth and Planetary Science Letters 183, 365–368.

Hu, R.Z., Burnard, P.G., Bi, X.W., Zhou, M.F., Peng, J.T., Su, W.C., Zhao, J.H., 2009. Mantle-derived gaseous components in ore-forming fluids of the Xiangshan uranium deposit, Jiangxi province, China: evidence from He, Ar and C isotopes. Chemical Geology 266, 86–95.

Lal, D., 1987. Production of ^{3}He in terrestrial rocks. Chemical Geology 66, 89–98.
Lamb, M.P., Dietrich, W.E., Aciego, S.M., DePaolo, D.J., Manga, M., 2008. Formation of Box Canyon, Idaho, by megaflood: implications for seepage erosion on Earth and Mars. Science 320, 1067–1070.
Licciardi, J., Kurz, M.D., Clark, P., Brook, E., 1999. Calibration of cosmogenic ^{3}He production rates from Holocene lava flows in Oregon, USA, and effects of the Earth's magnetic field. Earth and Planetary Science Letters 172, 261–271.
Licciardi, J.M., Kurz, M.D., Curtice, J.M., 2006. Cosmogenic ^{3}He production rates from Holocene lava flows in Iceland. Earth and Planetary Science Letters 246, 251–264.
Lifton, N., Caffee, M., Finkel, R., Schaefer, J., Stone, J., Goehring, B., Phillips, D., Oviatt, C.G., Rood, D., 2009. A new estimate of the spallogenic production rate of in situ cosmogenic ^{10}Be from lake Bonneville shoreline features, Promonotory Point, Utah. Geological Society of America Abstracts 41, 229.
Lifton, N.A., Jull, A.J.T., Quade, J., 2001. A new extraction technique and production rate estimate for in situ cosmogenic ^{14}C in quartz. Geochimica Et Cosmochimica Acta 65, 1953–1969.
Light, A., 1996. Amino acid paleotemperature reconstruction and radiocarbon shoreline chronology of the Lake Bonneville Basin, USA. PhD thesis, University of Colorado.
Malde, H.E., 1968. The catastrophic late Pleistocene Bonneville Flood in the Snake River plain, Idaho. Geological Society of America Professional Paper 596, 52.
Martel, D.J., Onions, R.K., Hilton, D.R., Oxburgh, E.R., 1990. The role of element distribution in production and release of radiogenic helium – the Carnmenellis Granite, Southwest England. Chemical Geology 88, 207–221.
Niedermann, S., Goethals, M.M., Pilz, P., 2009. Evidence for a high ^{3}He or low ^{10}Be production rate from cosmogenic nuclide cross-calibration. Geochimica et Cosmochimica Acta 73, A940.
Niishizumi, K., Imamura, M., Caffee, M., Southon, J.R., Finkel, R.C., McAninch, J., 2007. Absolute calibration of ^{10}Be AMS standards. Nuclear Instruments and Methods in Physics Research B 258, 403–413.
O'Connor, J.E., 1993. Hydrology, hydraulics, and geomorphology of the Bonneville flood. Geological Society of America Special Paper 274, 83.
Oviatt, C.G., 1991. Quaternary geology of the Black Rock Desert, Millard County, Utah. Utah Geological and Mineralogical Survey, Salt Lake City.
Oviatt, C.G., Currey, D.R., Sack, D., 1992. Radiocarbon chronology of Lake Bonneville, Eastern Great-Basin, USA. Palaeogeography Palaeoclimatology Palaeoecology 99, 225–241.
Patterson, D.B., Farley, K.A., McInnes, B., 1997. Helium isotopic composition of the Tabar-Lihir-Tanga-Feni island arc, Papua New Guinea. Geochimica et Cosmochimica Acta 61, 2485–2496.
Phillips, F., Stone, W.D., Fabryka-Martin, J.T., 2001. An improved approach to calculating low-energy cosmic ray neutron fluxes near the land/atmosphere interface. Chemical Geology 175, 689–701.
Poreda, R.J., Farley, K.A., 1992. Rare-gases in Samoan xenoliths. Earth and Planetary Science Letters 113, 129–144.
Putnam, A.E., Schaefer, J., Barrell, D.J.A., Vendergoes, M., Denton, G.H., Kaplan, M.R., Finkel, R.C., Schwartz, R., Goehring, B., Kelley, S.E., 2010. In situ cosmogenic ^{10}Be production-rate calibration from the Southern Alps, New Zealand. Quaternary Geochronology 5 (4), 392–409.
Reiners, P.W., Farley, K.A., Hickes, H.J., 2002. He diffusion and (U–Th)/He thermochronometry of zircon: initial results from Fish Canyon Tuff and Gold Butte. Tectonophysics 349, 297–308.
Rosgen, D.L., 1994. A classification of natural rivers. Catena 22, 169–199.
Scott, W.E., McCoy, W.D., Chroba, R.R., Rubin, M., 1983. Reinterpretation of the exposed record of the last two cycles of Lake Bonneville, Western United States. Quaternary Research 20, 261–285.
Vogel, T.A., Hidalgo, P.J., Patino, L.C., Tefend, K.S., Ehrlich, R., 2008. Evaluation of magma mixing and fractional crystallization using whole-rock chemical analyses: polytopic vector analyses. Geochemistry, Geophysics, Geosystems – G3 9. doi:10.1029/2007GC001790.
Wolf, R.A., Farley, K.A., Silver, L.T., 1996. Helium diffusion and low-temperature thermochronometry of apatite. Geochimica et Cosmochimica Acta 60, 4231–4240.
Ziegler, J.F., 2003. Stopping and Range of Ions in Matter (SRIM). http://www.srim.org.